Check for updates

CHEMISTRY

Molecular interfaces drive vertical crystallization in Dion-Jacobson perovskite solar cells

Rui Wang[1], Xiyue Dong[1], Yuting Ma[1], Liu Yang[2], Jiangnan Li[1], Yuping Gao[1], Yu Chen[3], Yu Zou[1], Wenjuan Feng[1], Ziyang Hu[2], Yongsheng Chen[1,4]*, Yongsheng Liu[1,4]*

Copyright © 2026 The Authors, some rights reserved; exclusive licensee American Association for the Advancement of Science. No claim to original U.S. Government Works. Distributed under a Creative Commons Attribution NonCommercial License 4.0 (CC BY-NC).

Two-dimensional perovskites are promising candidates for photovoltaics due to their intrinsic structural stability, but their efficiency is often limited by poor charge transport, in part due to unfavorable crystal orientation. Here, we report a molecular interface engineering strategy using dual-anchoring organic acids, croconic acid (CA) and squaric acid (SA), to direct vertical crystallization in Dion-Jacobson (DJ) perovskite films. These molecules form robust interlayers between the NiO_x hole transport layer and TTDMA (thieno[3,2-*b*]thiophene-2,5-diyldimethanaminium)–based DJ perovskites (nominal $n = 4$), with SA exhibiting ordered vertical orientation via bidentate coordination. This templated interface promotes vertical orientation, reduces interfacial defects and lattice strain, and suppresses Ni^{3+}-induced oxidation of I^-. As a result, devices incorporating SA achieve a champion power conversion efficiency of 22.03% (certified 21.42%) along with outstanding operational stability. This study demonstrates a general molecular interface strategy to direct vertical crystallization and improve the performance of layered perovskite solar cells.

INTRODUCTION

Two-dimensional (2D) metal halide perovskites have attracted intense interest for photovoltaic applications due to their superior intrinsic structural and environmental stability compared to their 3D counterparts (*1*–*5*). Among 2D perovskite families, Dion-Jacobson (DJ) phases that comprise divalent organic spacers directly connecting adjacent corner-sharing $[PbI_6]^{4-}$ layers offer improved mechanical rigidity by eliminating van der Waals gaps found in Ruddlesden-Popper (RP) phases. Despite recent advances, power conversion efficiencies (PCEs) of DJ perovskite solar cells (PSCs) still lag behind their 3D counterparts, (*6*–*14*) primarily due to strong excitonic effects and intrinsic anisotropic charge transport that hinder efficient carrier extraction (*15*).

Incorporating spacers with conjugated structure and/or large dipole moments has proven to be an effective strategy for reducing excitonic effects (*16*–*23*). Beyond this, a critical factor limiting performance is the crystallographic orientation of the 2D perovskite layers, where vertical alignment is essential for efficient out-of-plane charge transport and minimizing recombination losses (*24*). To date, strategies to achieve vertical orientation have primarily focused on processing techniques, such as hot-casting, solvent engineering, and the incorporation of additives (*24*–*30*). A landmark study by Mohite and colleagues. demonstrated that hot-casting method could induce vertical orientation in RP perovskites, achieving a notable PCE of 12.52% with remarkable stability (*24*). This work catalyzed broad interest in morphological control for 2D perovskite films. Additives such as MACl and NH_4SCN have since been used to modulate the crystallization kinetics and promote vertical alignment (*26*, *27*). However, molecular-level strategies at the buried bottom interface to direct such vertical crystallization remain underexplored.

Here, we present a molecular interface engineering strategy that directs vertical crystallization in DJ perovskite films and markedly boosts device performance. Specifically, two dual-anchoring molecules, croconic acid (CA) and squaric acid (SA), were explored as functional interlayer between NiO_x hole transport layer (HTL) and DJ perovskite layer based on thieno[3,2-*b*]thiophene-2,5-diyldimethanaminium (TTDMA). These molecules exhibit strong interactions with both the NiO_x surface and the overlying DJ perovskite. Notably, although CA forms a twisted, disordered layer due to multivalent coordination with NiO_x, SA adopts an ordered vertical orientation via bidentate coordination, effectively serving as a molecular template that guides perovskite nucleation and vertical growth. This templating effect promotes the formation of highly crystalline of (TTDMA)$(MA_{0.4}FA_{0.6})_{n-1}Pb_nI_{3n+1}$ (TTDMA-Pb, nominal $n = 4$) films with well-defined vertical orientation. In addition to structural regulation, the SA interface layer simultaneously passivated interface defects, relieves lattice stress, aligns interface energy levels, and suppresses Ni^{3+}-induced I^- oxidation. As a result, devices incorporating SA achieve a record PCE of 22.03% (certified 21.42%) for DJ PSCs, along with superior operational stability. The universality of this method that directs vertical crystallization was further validated in RP perovskites using thieno[3,2-*b*]thiophen-2-ylmethanaminium (TTMA) as the spacer.

RESULTS

Functional organic molecules with dual-anchoring properties

The molecular structure of SA and CA are illustrated in Fig. 1A. Both contain multiple carbonyl (—C═O) and hydroxyl (—OH) groups capable of interacting with both NiO_x and the perovskite layer in inverted PSCs. First-principles density function theory (DFT) calculations (fig. S1A) reveal that the —C═O group exhibits a larger binding energy (E_b) when adsorbed onto the NiO_x surface, indicating a stronger interaction with undercoordinated Ni sites. As a result, SA preferentially adopts a vertical orientation on the NiO_x surface via bidentate coordination through two C═O···Ni bonds (Fig. 1A). In contrast, CA forms a twisted configuration due to its three C═O···Ni

[1]State Key Laboratory of Elemento-Organic Chemistry, the Centre of Nanoscale Science Technology and Key Laboratory of Functional Polymer Materials, Frontiers Science Center for New Organic Matter, College of Chemistry, Nankai University, Tianjin 300071, China. [2]Department of Microelectronic Science and Engineering, Ningbo University, Ningbo 315211, China. [3]Institute of High Energy Physics, Chinese Academy of Sciences, Beijing 100049, China. [4]Haihe Laboratory of Sustainable Chemical Transformations, Tianjin 300192, China.
*Corresponding author. Email: yschen99@nankai.edu.cn (Y.C.); liuys@nankai.edu.cn (Y.L.)

Downloaded from https://www.science.org on June 07, 2026

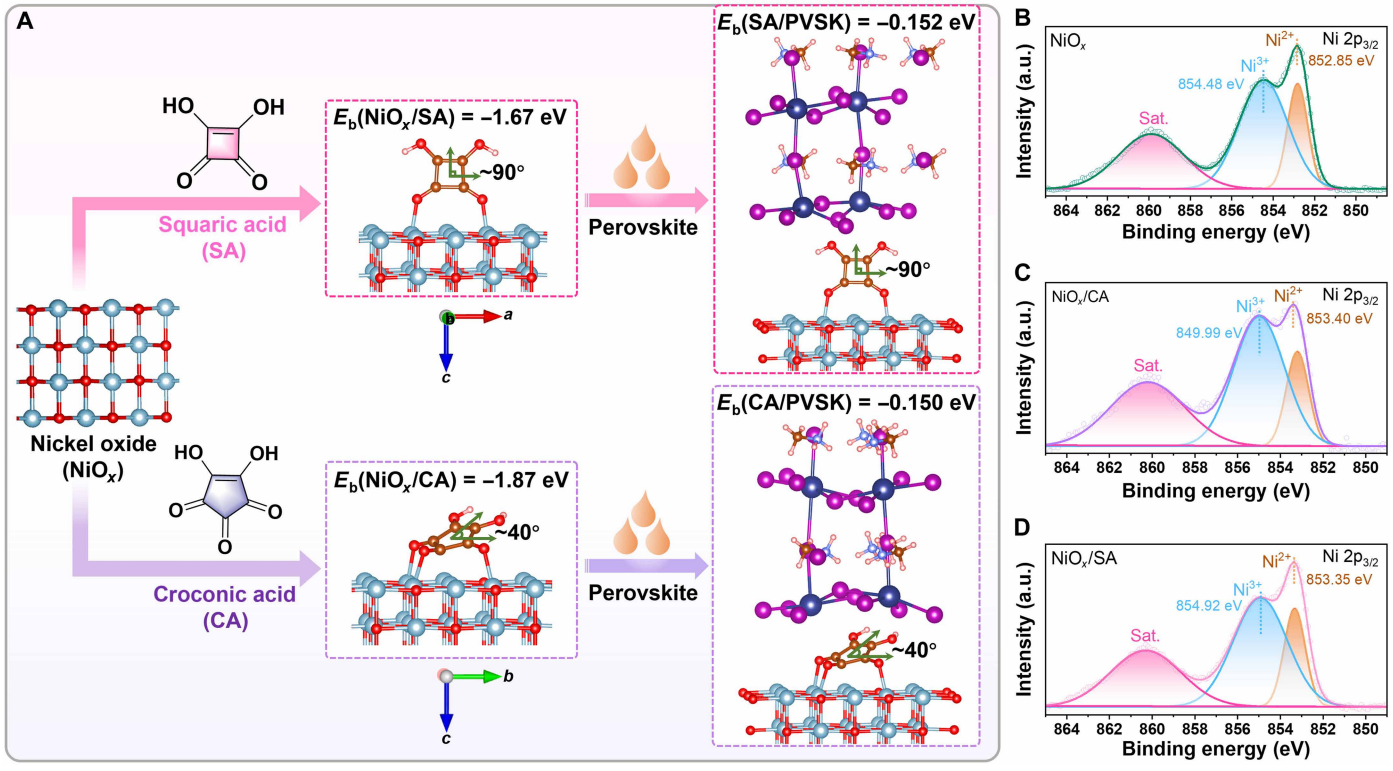

Fig. 1. Dual-anchoring properties of functional organic molecules. (**A**) Chemical structure and the optimal conformation for SA and CA adsorption at the interface between perovskite (PVSK) and NiO_x. (**B** to **D**) XPS spectra of Ni $2p_{3/2}$ for NiO_x, NiO_x/CA, and NiO_x/SA. a.u., arbitrary units.

interactions, leading to a less ordered interface (Fig. 1A and fig. S1B). Compared to CA, the vertical orientation of SA molecules reduces steric hindrance and allows for higher molecular packing density (Fig. 1B and fig. S2). This enhanced packing leads to smoother surfaces and reduced surface potential differences, as verified by atomic force microscopy (AFM) and conductive AFM (c-AFM) analyses (figs. S3 and S4). Moreover, the NiO_x/SA film exhibits a smaller water contact angle than NiO_x and NiO_x/CA (fig. S5), indicating improved hydrophilicity. This enhanced wettability facilitates better interaction with the perovskite precursor solution, promoting uniform film formation and improved crystallization as discussed below.

Benefiting from the robust coordination between the —C═O groups and the NiO_x surface, both CA and SA molecules can form robust self-assembled monolayers (SAMs) that are not easily removed by dimethyl sulfoxide (DMSO)–based perovskite precursor solution, as confirmed by ultraviolet-visible (UV-Vis) absorption spectra (fig. S6). The optimal dual-anchoring interactions of CA (and SA) between NiO_x and perovskite are illustrated in Fig. 1A. Both SA and CA prefer to absorb on the NiO_x surface via C═O···Ni interactions, exposing —OH groups that subsequently interact with the overlying 2D perovskite layer. Notably, DFT calculations show that the O—Pb bond lengths between SA and the perovskite is at the range of 3.22 to 3.32 Å, which are narrower and more uniform than those CA (2.77 to 3.64 Å), indicating more homogeneous bonding with the perovskite (fig. S7). Furthermore, the molecular spacing of adjacent SA molecules (5.96 Å) is more compatible with the perovskite lattice (6.21 Å) compared to CA (6.67 Å) (*31*, *32*). This better lattice match can enhance the anchoring and adsorption of SA onto the perovskite through chemical interactions while also guiding the alignment of perovskite crystals, thereby promoting a vertical orientation (*31*). Furthermore, the —OH groups of SA exhibit a larger binding energy with perovskite (E_b = −0.152 eV) than CA (E_b = −0.150 eV), suggesting that SA is more effective in anchoring the perovskite crystals, passivating defects, and regulating the crystallization and orientation (*33*).

The interaction between SA/CA and the NiO_x layer were further supported by x-ray photoelectron spectroscopy (XPS) (Fig. 1, B to D). After SA modification, the Ni $2p_{3/2}$ peaks at 852.85 eV (Ni^{2+}) and 854.48 eV (Ni^{3+}) shifted to 853.35 eV (Ni^{2+}) and 854.92 eV (Ni^{3+}), respectively, consistent with coordination between Ni and the functional groups of SA. A similar trend was observed for CA. Fourier transform infrared (FTIR) spectra (figs. S8, A and B) show that the —C═O stretching vibration peaks exhibit more pronounced shifts than —C—O, indicating stronger interaction between NiO_x and —C═O than with —OH. Upon addition of PbI_2, the —C—O stretching vibrations show a pronounced shift (fig. S8, C and D), indicating strong interactions with PbI_2, consistent with DFT results (*34*).

Crystal growth and orientation directed by interfacial molecules

We performed in situ photoluminescence (PL) measurements of TTDMA-Pb films on various substrates to investigate the impact of functional molecules on perovskite crystallization (Fig. 2, A to F). At 40°C for 120 s (Fig. 2, A to C), the TTDMA-Pb film deposited on NiO_x/CA exhibits an initial PL emission at ~750 nm after ~105 s, occurring earlier than those on indium tin oxide (ITO)/NiO_x (~114 s) and ITO/NiO_x/CA (~108 s) substrates. This observation further confirms accelerated nucleation as the vertically aligned, densely packed SA layer provides a high density of uniform nucleation sites (—OH

Downloaded from https://www.science.org on June 07, 2026

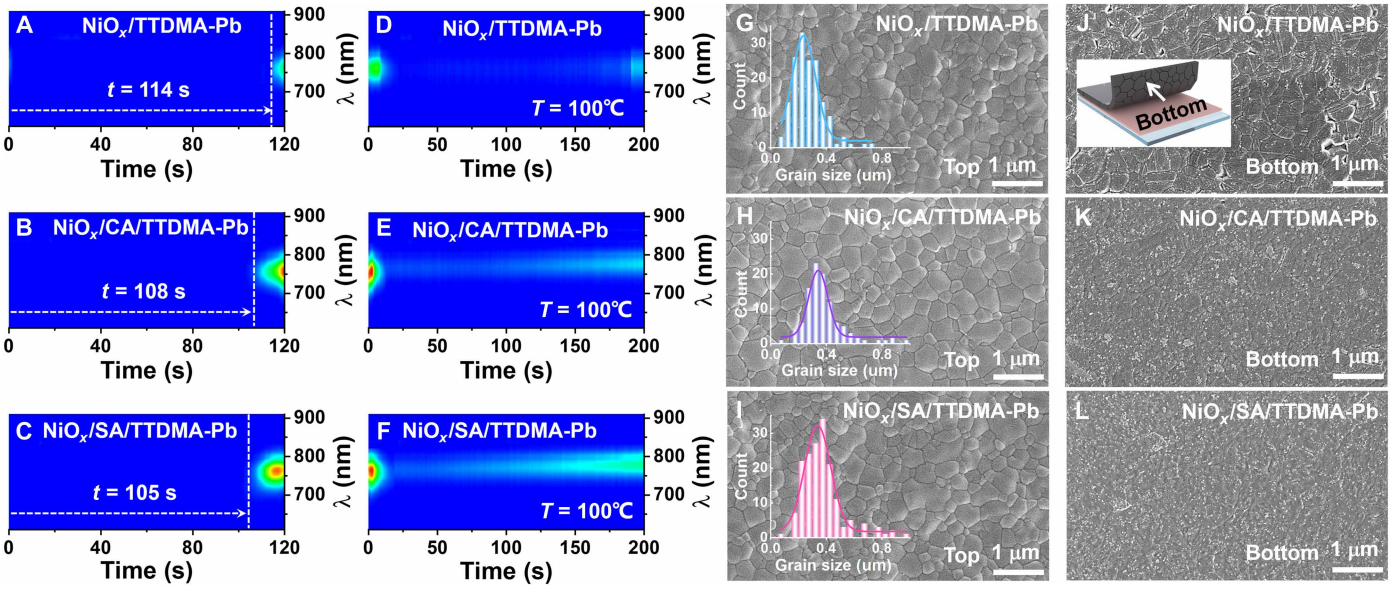

Fig. 2. Functional molecules guide the crystallization and morphology control of DJ perovskites. (**A** to **C**) In situ PL spectra of TTDMA-Pb films on different substrates at 40°C. (**D** to **F**) In situ PL spectra of TTDMA-Pb films on different substrates at 100°C. (**G** to **I**), Top morphologies of TTDMA-Pb films deposited on different substrates (insets are grain size distribution). (**J** to **L**) Bottom morphologies of TTDMA-Pb films deposited on NiO_x, NiO_x/CA, and NiO_x/SA substrates.

coordination sites) that facilitate the initial assembly of perovskite precursors, whereas its enhanced wettability (fig. S5) lowers the heterogeneous nucleation barrier (*35*). During subsequent annealing at 100°C for 200 s (Fig. 2, D to F), the PL intensity underwent a characteristic evolution: an initial increase, followed by a decrease, and then a final increase. This trend signifies a crystallization-dissolution-recrystallization process (*36*). Notably, SA substantially narrows the kinetic window for recrystallization following surface crystal dissolution, promoting perovskite recrystallization and improving crystalline quality.

To evaluate the impact of substrate modification on the film quality of TTDMA-Pb, top-view scanning electron microscopy (SEM) measurements were performed. As shown in Fig. 2 (G to I), TTDMA-Pb films deposited on ITO/NiO_x substrates modified with CA or SA exhibit obviously increased grain size compared to that on unmodified ITO/NiO_x. Notably, the film on the ITO/NiO_x/SA substrate displays a pronounced vertical growth with large, monolithic grains (fig. S9), which facilitate efficient charge transport between top and bottom electrodes. To gain deeper insights into the effects of SA and CA on the morphology of DJ perovskites, we obtained the SEM images of the buried bottom surfaces of TTDMA-Pb films. These surfaces were exposed by peeling off the perovskite layers using solidified adhesive. As depicted in Fig. 2 (J to L), the bottom surface of NiO_x/TTDMA-Pb films exhibits obvious pinholes compared to the top surface. Notably, the bottom surfaces of the film on bare NiO_x exhibits noticeable pinholes, indicative of poor interfacial coverage. In contrast, films deposited on ITO/NiO_x substrates modified with CA or SA show notably improved bottom surface uniformity with minimal pinhole formation. In addition, a higher density of small NiO_x particles was observed on the bottom surface of the film grown on CA or SA modified substrates compared to the unmodified control substrate. This indicates a strong interfacial interaction between the dual-anchoring molecules and both TTDMA-Pb and NiO_x, consistent with the DFT calculation results. Note that we repeated the peeling and SEM characterization on multiple samples (fig. S10) and consistently observed these features, indicating that they predominantly originate from intrinsic perovskite-substrate properties rather than from SEM preparation artifacts.

To investigate the depth-dependent crystallization behavior of TTDMA-Pb films, grazing incidence wide-angle x-ray scattering (GIWAXS) measurements were performed at various incident angles. As shown in Fig. 3 (A to C), the as-deposited wet films on different substrates exhibit a mixed-phase composition, comprising both the perovskite phase ($q \approx 1$ Å^{-1}) and an intermediate phase ($q \approx 0.5$ Å^{-1}), extending from the film surface into the bulk (*37*). Upon annealing, the intermediate phase gradually transforms into the perovskite phase. Notably, for films deposited on bare NiO_x, crystallinity progressively decreases from the surface to the buried interface (fig. S11, A to C). In contrast, the incorporation of CA or SA at the TTDMA-Pb/NiO_x interface substantially enhances perovskite crystallinity in the buried region, suggesting that interfacial functional molecules promote nucleation and improve film quality, consistent with the in situ PL results. To gain deeper insight into the orientation distribution of DJ perovskites, azimuth angle plots were derived by integrating the diffraction intensity along the (111) ring ($q = 0.9$ to 1.1 Å^{-1}). As depicted in Fig. 3 (D to F), at a low incident angle of 0.1°, all TTDMA-Pb films exhibit preferred orientation at a polar angle (χ) of 0°, indicating an intrinsic tendency for vertical alignment at the surface, likely driven by the self-assembly of TTDMA spacer cations. With increasing incident angle (0.7° to 0.9°), the TTDMA-Pb film deposited on bare NiO_x exhibits increased diffraction intensity at $40° < \chi < 90°$ (Fig. 3D), suggesting the tilted crystal orientation at the buried interface. In addition, a broader orientation distribution emerges with progressive solvent evaporation (fig. S11D), implying increased disorder during film solidification. In contrast, films deposited on CA-modified NiO_x exhibit a predominantly vertical

Downloaded from https://www.science.org on June 07, 2026

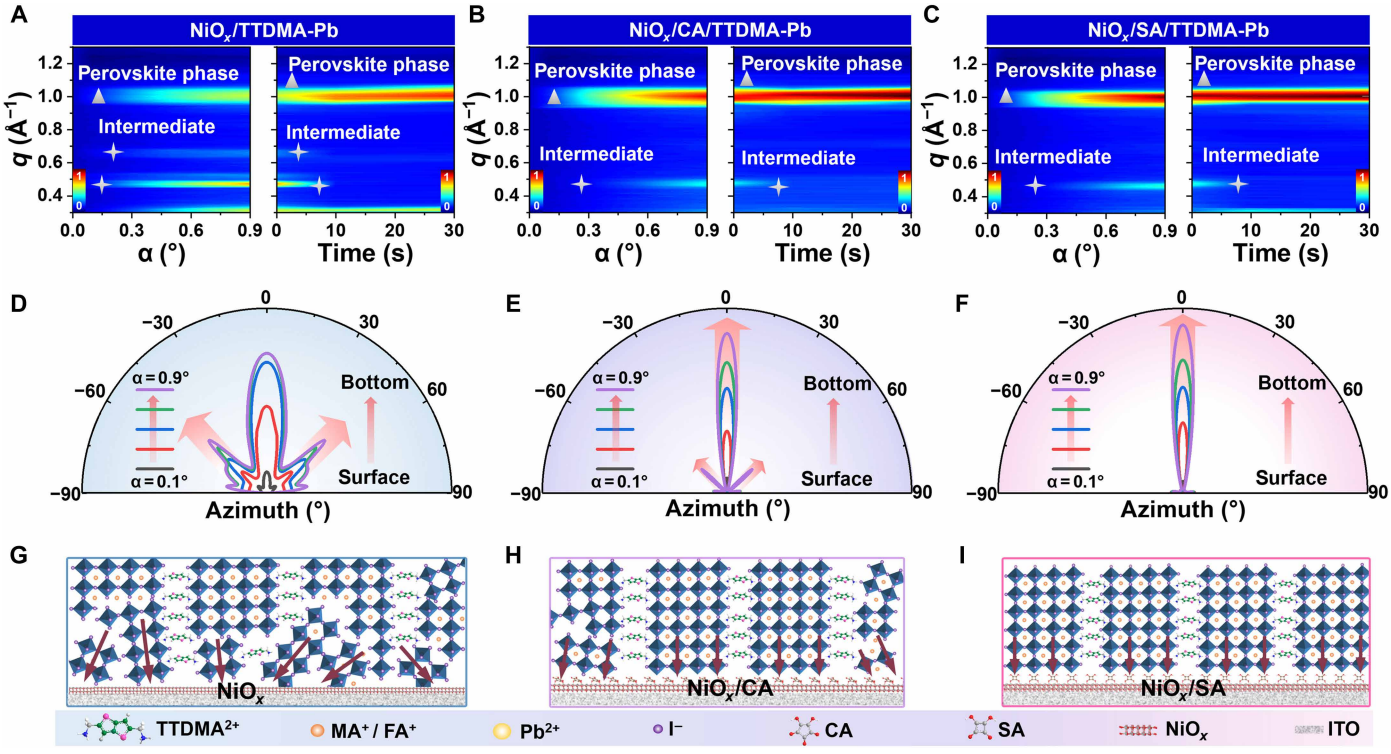

Fig. 3. Crystal growth and orientation of DJ perovskites. (**A** to **C**) Incident angle–dependent GIWAXS of TTDMA-Pb films on different substrates (left), along with their respective GIWAXS (T = 100°C) with an incident angle of 0.9° (right). (**D** to **F**) Radially integrated intensity plots along the (111) rings of TTDMA-Pb films on NiO_x (D), NiO_x/CA (E), and NiO_x/SA (F). (**G** to **I**) Schematic illustrations of the crystal orientation of TTDMA-Pb on different substrates.

orientation ($\chi = 0°$) with a minor fraction of tilted grains ($\chi = 50°$) at the buried interface (Fig. 3E and fig. S11E). Notably, the SA-modified substrate leads to highly oriented vertical crystallization throughout the film, as evidenced by a sharp, dominant diffraction signal at $\chi = 0°$, which intensifies as solvent evaporation proceeds. (Fig. 3F and fig. S11F).

These findings demonstrate that dual-anchoring functional molecules effectively drive the transition from randomly oriented to vertically aligned crystal growth in DJ perovskites. This underlying mechanism is further supported by combining the aforementioned DFT calculations and in situ PL results. As illustrated in Fig. 3G and figs. S12 and S13, in the absence of interfacial modulation, the isotropic environment at the buried bottom interface favors random crystal orientations (*38*). The introduction of CA molecules establishes a more ordered interfacial environment, enhancing alignment but still allowing for some degree of misorientation due to twisted CA on the NiO_x surface (Fig. 3H). In contrast, SA molecules, owing to their compact structure and minimal steric hindrance, achieve higher surface coverage and vertical alignment on NiO_x. Through bidentate coordination between their hydroxyl groups and Pb^{2+} ions, SA molecules stabilize local Pb^{2+} concentrations near the interface, promoting heterogeneous nucleation. Furthermore, the lattice matching between SA and perovskite facilitates epitaxial growth, leading to the formation of vertical orientated and high-quality TTDMA-Pb films (Fig. 3I).

Electronic properties and lattice stress of perovskite films

To investigate the impact of CA and SA on the electronic properties of NiO_x, we conducted kelvin probe force microscopy (KPFM) and ultraviolet photoelectron spectroscopy (UPS) measurements. The KPFM results in Fig. 4 (A to C) show a sequential decrease in average surface potential from −46.7 mV for pristine NiO_x to −139.1 and −209.5 mV for NiO_x/CA and NiO_x/SA, respectively. This trend is consistent with the downward shift in Fermi level (E_F) for the corresponding films, as confirmed by UPS (fig. S14) (*39*–*41*). The E_F values are −4.26 eV for NiO_x, −4.46 eV for NiO_x/CA, and −4.65 eV for NiO_x/SA, with the corresponding valence band maximum (VBM) of −5.22, −5.39, and −5.49 eV, respectively. Consequently, the E_F-VBM energy gap narrows from 0.96 eV (NiO_x) to 0.93 eV (NiO_x/CA) and further to 0.84 eV (NiO_x/SA). The reduced E_F-VBM energy gap could promote the excitation of electron in valence band to the conduction band, leading to increased hole concentration and conductivity of the NiO_x film.

Figure 4 (D to F) illustrate the energy band alignment at the NiO_x/TTDMA-Pb interface with and without interfacial molecular modification. The E_{VBM} offset (ΔE) between TTDMA-Pb and NiO_x is reduced from initial 0.32 eV (pristine) to 0.15 eV with CA and further to 0.05 eV with SA. This progressive alignment enhancement facilitates more efficient hole extraction and transport, contributing to improvements in both open-circuit voltage (V_{OC}) and short-circuit current density (J_{SC}) as discussed below (*42*). Steady-state PL and time-resolved PL (TRPL) measurements further confirm this behavior (fig. S15 and table S1). TTDMA-Pb films on CA-modified and SA-modified NiO_x exhibit stronger PL quenching and shortened carrier lifetimes, indicating more efficient hole extraction from TTDMA-Pb to the HTL. We note that the nominal $n = 4$ composition inherently forms a heterogeneous phase distribution (fig. S15),

Downloaded from https://www.science.org on June 07, 2026

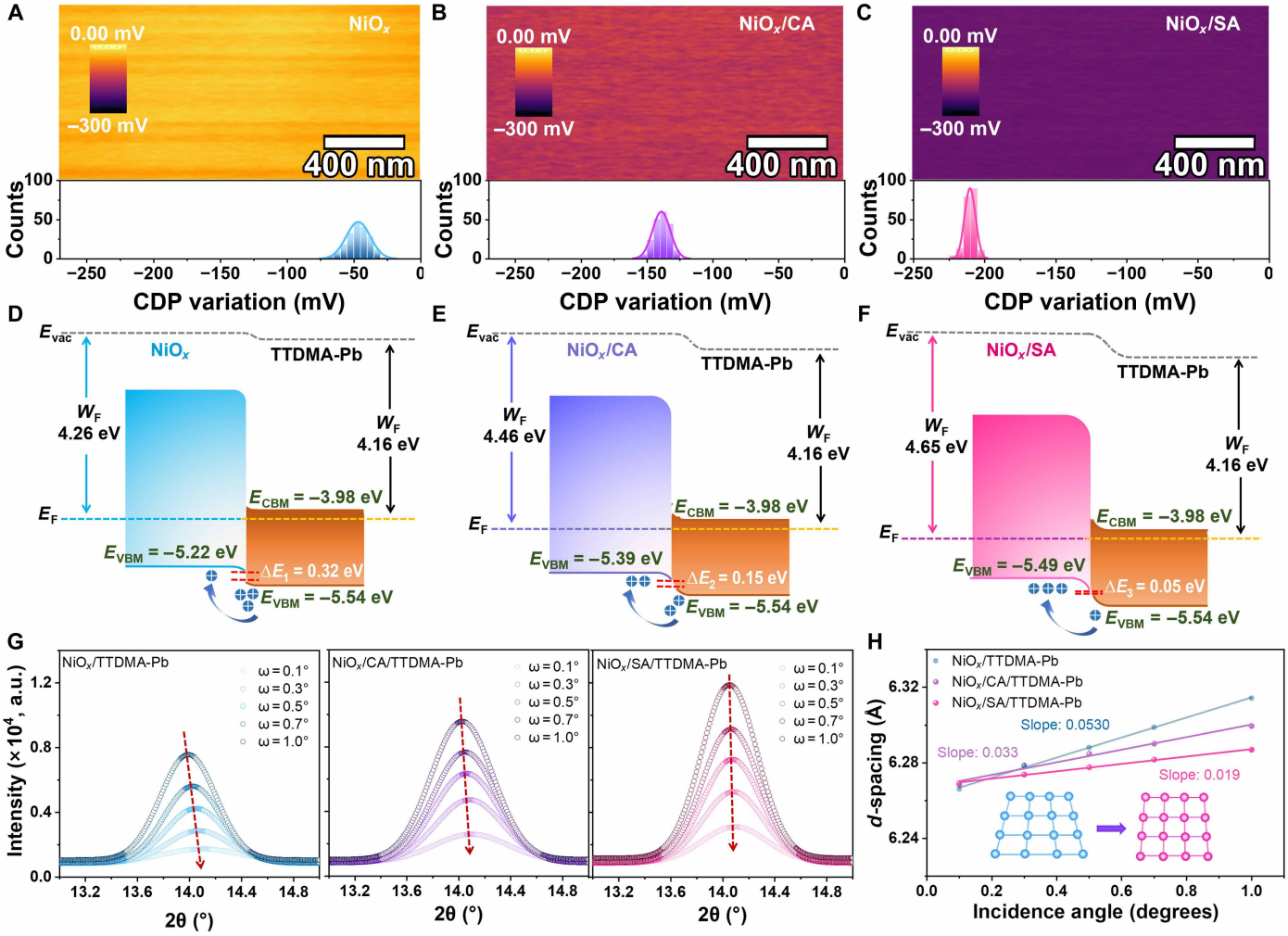

Fig. 4. Electronic properties of perovskite films. (**A** to **C**) KPFM images and statistical potential distributions of NiO_x, NiO_x/CA, and NiO_x/SA films. (**D** to **F**) Energy diagram of NiO_x, NiO_x/CA, NiO_x/SA, and TTDMA-Pb films. (**G**) GIXD spectra for TTDMA-Pb films on different substrates at different tilt angles. (**H**) *d*-spacing values obtained from the (111) plane as a function of incidence angle.

consistent with the literature report on solution-processed quasi-2D perovskites (*43*).

Residual stress within perovskite films can compromise structural integrity and device longevity (*44*). To evaluate the effect of substrate properties on strain relaxation, we conducted grazing incidence x-ray diffraction (GIXD) measurements. As depicted in Fig. 4 (G and H), increasing the grazing incidence angle (ω) lead to a gradual shift of the (111) diffraction peak toward smaller angles in the NiO_x/TTDMA-Pb film, indicating lattice expansion and stress accumulation (*33*). In contrast, this shift is evidently attenuated in CA-modified and SA-modified samples. The slopes of the *d*-spacing versus ω curve decreased from 0.053 (NiO_x/TTDMA-Pb) to 0.033 (CA-modified) and 0.019 (SA-modified), confirming a reduction in residual stress. These results suggest that dual-anchoring molecules promote strain relaxation during crystallization, with SA being more effective due to its superior lattice matching with the perovskite phase.

Photovoltaic performance

To evaluate the photovoltaic performance of TTDMA-Pb-based DJ PSCs, we fabricated inverted devices using NiO_x, NiO_x/CA, and NiO_x/SA as HTLs. The detailed photovoltaic parameters are summarized in table S2. Note that SA and CA do not function as effective SAM layers on bare ITO, and their beneficial effects arise only when they modify and passivate the NiO_x surface, which facilitates efficient hole extraction and promotes improved perovskite nucleation and orientation. In addition, for the CA and SA deposition, we used spin-coating followed by an optimized annealing step (100°C for 3 min) to allow the molecules to form well-ordered interfacial layers on NiO_x (fig. S16). As shown in Fig. 5A, the reference device using pristine NiO_x exhibits a V_{OC} of 1.09 V, a J_{SC} of 23.11 mA cm^{-2}, and a fill factor (FF) of 77.05%, achieving a PCE of 19.41%. After using CA as dual anchoring interfacial layer, the PCE was increased to 20.31%, with a V_{OC} of 1.12 V, a J_{SC} of 23.25 mA cm^{-2}, and an FF of 77.99%. The SA-based device shows a record-breaking PCE of 22.03%, with a J_{SC} of 23.78 mA cm^{-2}, a V_{OC} of 1.14 V, and a notable FF of 81.26%. This marks a substantial breakthrough for DJ PSCs (Fig. 5B). The NiO_x/SA/TTDMA-Pb devices show excellent reproducibility and yield a certified PCE of 21.42% with negligible hysteresis (figs. S17 to S20). Note that this is the highest certified efficiency reported thus far for quasi-2D PSCs to the best of our knowledge

Downloaded from https://www.science.org on June 07, 2026

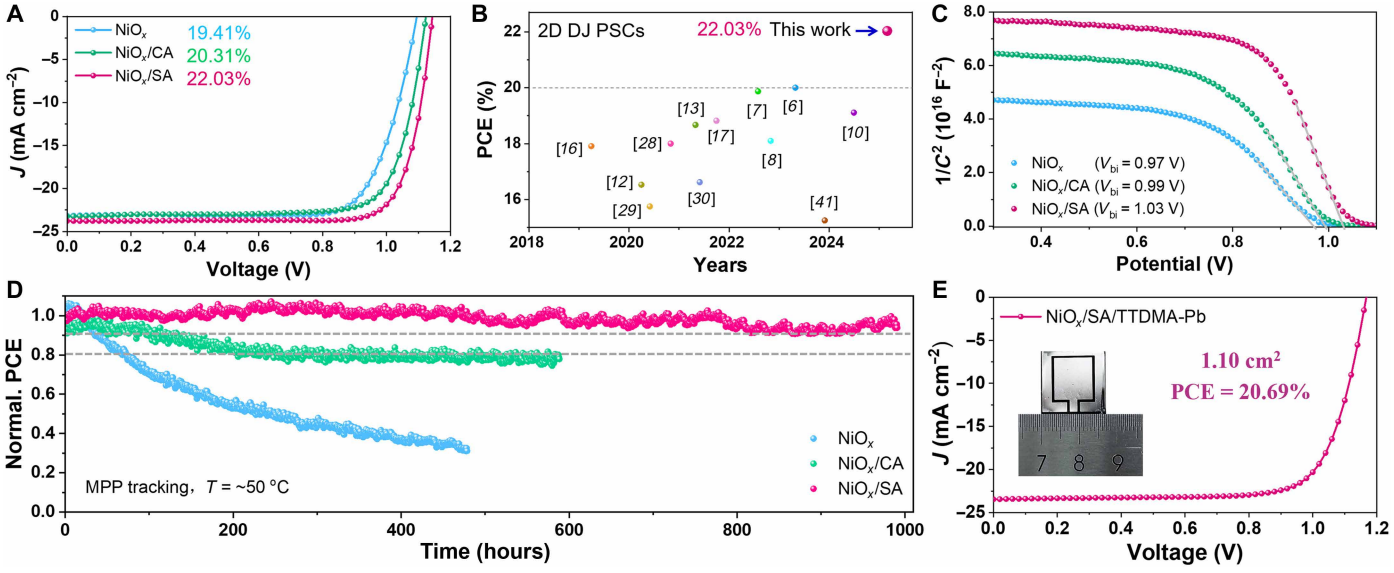

Fig. 5. Device photovoltaic performance. (**A**) *J-V* curves of optimized TTDMA-Pb devices with or without functional layers. (**B**) Summary of efficiency (>15%) from previously published results on DJ PSCs (average $n < 6$) and this study. (**C**) Mott-Schottky plots of the corresponding devices. (**D**) MPP tracking of the unencapsulated devices under continuous light illumination at ~50°C in N_2. (**E**) *J-V* curve of the device based on SA with an area of 1.1 cm^2.

(table S3) (*7*–*9*, *14*, *16*, *19*, *26*, *29*, *30*, *45*–*64*). The successively enhancement in V_{OC} from 1.09 V (control) to 1.12 V (CA modified) and 1.14 V (SA modified) correlates with an increase in built-in potential (V_{bi}) obtained from *C-V* measurement (Fig. 5C) (*65*). The superior efficiency of the SA-based device was further validated by the steady-state power output measurement (PCE_{max} = 21.79%) at the max power point under 0.98-V bias (fig. S19B). In addition, the J_{SC} integrated from the external quantum efficiency (EQE) spectra are 23.16, 23.25, and 23.78 mA cm^{-2} for the corresponding devices, respectively, matching well with *J-V* results (fig. S19C).

Light intensity–dependent J_{SC} measurements reveal reduced bimolecular recombination in the SA-based device, evidenced by a near-unity power-law exponent ($\alpha = 0.995$), compared to CA-based (0.991) and control (0.989) devices (fig. S19A) (*66*). Similarly, the V_{OC} versus light intensity plot (fig. S21B) shows a reduced slope for the SA-based device (1.47 kT/q) compared to CA-based (1.58 kT/q) control (1.66 kT/q) devices, indicating lower trap-assisted recombination (*67*). These findings are corroborated by reduced trap density (fig. S21C), prolonged photovoltage decay (fig. S22A), and enhanced hole mobility (fig. S22B).

The interfacial instability arising from the redox reaction between I^- and Ni^{3+} presents a notable challenge in achieving the high efficiency and stability of quasi-2D PSCs (*68*, *69*). XPS analysis on both as-deposited and aged NiO_x films were performed (fig. S23, A and B). Aged films were prepared by depositing the TTDMA-Pb perovskite on NiO_x, aging under light-emitting diode (LED) illumination (100 mW cm^{-2}, T = 40°C) for 5 days and then washing with *N*,*N*′-dimethylformamide (DMF) to expose the NiO_x surface. The aged NiO_x film shows a large drop in Ni^{3+}/Ni^{2+} ratio from 3.17 to 1.71 for unmodified NiO_x, indicating I^- induced Ni^{3+} reduction. In contrast, this ratio remains higher for NiO_x/CA (from 3.32 to 2.49) and NiO_x/SA (from 3.66 to 3.13), confirming the superior protective effect of the dense SA layer on the overlying perovskite film. UV-Vis absorption of toluene extracts after light soaking further confirms suppressed I^- oxidation in CA-modified and SA-modified films (fig. S23). Moreover, x-ray diffraction (XRD) tracking under ambient conditions reveals the emergence of PbI_2 and low *n*-value phases in the control and CA-based film after aging, whereas SA-modified film remains undecomposed even after 360 hours (fig. S24). These results indicate that the dense SA interlayer effectively mitigates the I^-/Ni^{3+} redox reaction, preserving a higher Ni^{3+}/Ni^{2+} ratio and suppressing I^- oxidation, thereby stabilizing the perovskite/NiO_x interface and enhancing device durability.

The operational stability is substantially improved with interface engineering. Under maximum power point (MPP) tracking (LED, 100 mW cm^{-2}, N_2), the unencapsulated bare NiO_x-based device dropped to ~32% of its initial PCE after 470 hours. In contrast, devices modified with CA and SA maintained over 80 and 90% of their initial efficiencies after 580 and 990 hours, respectively (Fig. 5D). Note that the 85°C thermal aging results indicate that the SA-modified and CA-modified devices also have substantially improved thermal stability relative to the control (fig. S25). To further evaluate film uniformity, PSCs based on SA with active areas of 1.10 cm^2 were also fabricated. As shown in Fig. 5E, the best-performing device exhibited a V_{OC} of 1.17 V, a J_{SC} of 23.46 mA cm^{-2}, and an FF of 75.38%, delivering a high PCE of 20.69%. These results highlight the dual role of the SA interlayer in enhancing both efficiency and operational stability by improving crystallinity, suppressing charge recombination, and preventing interface degradation. Notably, the universality of this molecular interface engineering strategy in directing the vertical crystallization of DJ perovskite films was further demonstrated in the RP perovskite system by using TTMA as the spacer (figs. S26 and S27). This result highlights the broader applicability of the approach across different quasi-2D perovskite frameworks.

DISCUSSION

We have demonstrated molecular-scale regulation of DJ perovskite films by the incorporation of dual-anchoring organic functional

Downloaded from https://www.science.org on June 07, 2026

molecules (CA and SA) at the buried interface between NiO_x and TTDMA-Pb. Although CA forms a twisted configuration on NiO_x, SA assembles into an ordered, vertical aligned interlayer that more efficiently guides vertical crystal orientation, leading to enhanced energy level alignment, mitigated lattice stress, and suppressed Ni^{3+}-induced oxidation of I^-. DJ perovskite devices incorporating SA achieves a champion efficiency of 22.03% (certified 21.42%) and improved operational stability. These results highlight the potential of interfacial molecular engineering to control crystal growth in layered perovskites and advance the performance of quasi-2D PSCs.

MATERIALS AND METHODS

Materials

All the reagents and chemicals were used as received without further purification, including PbI_2 (99.999%, TCI), poly (3,4-ethylenedioxythiophene) polystyrene sulfonate (PEDOT:PSS, Baytron PVPAI 4083), phenyl-C61-butyricacidmethylester (PCBM; >99.5%, Advanced Election Technology Co. Ltd.), 2,9-dimethyl-4,7-diphenyl-1,10-phenanthroline (BCP, 96%), DMSO (99.8%, Alfa Aesar), isopropanol (IPA; AR, Aladdin Industrial Corporation), chlorobenzene (CB; Sigma-Aldrich), CA and SA (≥99%, Bide Pharmatech Co. Ltd.), DMF (J&K), and nickel oxide (NiO_x, 99.999%, Advanced Election Technology Co. Ltd.).

Device fabrication

The 2D RP perovskite $(TTMA)_2(MA_{0.4}FA_{0.6})_3Pb_4I_{13}$ (nominal $n = 4$) precursor solutions were prepared using a stoichiometric molar ratio of 2:1.2:1.8:4 for TTMAI, MAI, FAI, and PbI_2, respectively, dissolved in DMSO/DMF (4:6, v/v), with a Pb^{2+} concentration of 1.2 M. MACl was added to the precursor solution with a MACl/MAI weight ratio of 1:1. The 2D DJ perovskite $(TTDMA)(MA_{0.4}FA_{0.6})_3Pb_4I_{13}$ (nominal $n = 4$) precursor solutions were prepared using a stoichiometric molar ratio of 1:1.2:1.8:4 for TTDMAI, MAI, FAI, and PbI_2, respectively, dissolved in DMSO/DMF (8:2, v/v), with a Pb^{2+} concentration of 1.4 M. The MACl was added to the precursor solution with a MACl/MAI weight ratio of 1:1. The optimized concentration of SA or CA solution is 2 mg/ml in IPA. The inverted PSCs were fabricated on ITO-coated glass substrates. The ITO substrates were sequentially cleaned in distilled water, acetone, and IPA, followed by UV-ozone treatment. The NiO_x (25 mg/ml in H_2O) was spin coated on ITO at 5000 rpm for 30 s and annealed in air at 150°C for 15 min. After cooling, the substrates were transferred into a N_2-filled glove box. The SA or CA solution was spin coated on NiO_x at 8000 rpm for 30 s and annealed at 100°C for 3 min. After cooling to room temperature, the substrates were rinsed with IPA by spin-coating at 8000 rpm for 30 s. Subsequently, the DJ perovskite precursor solution was spin coated at 7000 rpm for 50 s. During the spin-coating process, 120 μl of the antisolvent (IPA/CB = 1:1, v/v) was dropped onto the spinning substrate at 20 s before the end of the procedure. The resulting TTDMA-Pb films were annealed at 100°C for 35 min. Afterward, the samples were transferred to a glove box and a $PC_{61}BM$ solution (20 mg/ml in CB) was spin coated on the top of the samples at 1200 rpm for 40 s, followed by deposition of a BCP layer (0.6 mg/ml in IPA) at 1000 rpm for 40 s. Last, a 100-nm silver electrode was thermally deposited under a vacuum of 1×10^{-4} Pa. The effective area of the devices were 0.1 cm^2 for small-area devices and 1.10 cm^2 for large-area devices defined by shadow masks.

Film characterization

SEM images was obtained using the ZEISS MERLIN Compact at the accelerating voltage of 5 kV. XRD measurements were performed using a Rigaku Ultima IV x-ray powder diffractometer with Cu Kα radiation (λ = 1.54 Å) with a 2θ range of 3° to 50° at a scan rate of 20° min^{-1}. Optical absorption spectra of the perovskite films were obtained using a Cary 5000 UV-visible-NIR spectrophotometer. Steady-state PL and TRPL measurements were performed by an FLS1000 spectrometer (Edinburgh Instruments Ltd.) with an excitation wavelength of 450 nm. XPS and UPS measurements were carried out using the Thermo ESCALAB 250XI. KPFM was carried out with an Asylum Research Cypher atomic force microscope equipped with a silicon probe coated with Ti/Ir (ASYELEC-01-R2), with a force constant of 0.5 to 4.4 nN/nm and a tip radius of 28 nm. The Nap mode was used, consisting of two passes: the first pass acquired surface topography in tapping mode, whereas the second pass lifted the first 40 nm above the surface and acquired the potential offset between the tip and the sample through a dc voltage feedback loop. All AFM measurements were carried out under ambient conditions with a relative humidity of ~20%.

In situ PL

In situ PL measurements were performed using a custom-built setup. The quasi-2D perovskite films were excited by a wavelength-tunable laser (λ = 450 nm), and the emitted PL was collected using a fiber-coupled spectrometer covering a spectral range of 400 to 1000 nm. Samples were placed in a temperature-controlled (40° and 100°C) chamber, regulated by a temperature control console (TU-300) with an accuracy of ±0.5°C.

GIWAXS measurements

Angle-dependent GIWAXS measurements were performed using a Xeuss 3.0 instrument (Xenocs, France) equipped with an x-ray source (λ = 1.54189 Å). These measurements were conducted on quasi-2D perovskite films deposited on various substrates during thermal annealing at 100°C (0 to 30 s). The GIWAXS pattern of the postannealed quasi-2D perovskite films were additionally obtained at the 1W1A Diffuse X-ray Scattering Station of Beijing Synchrotron Radiation Facility (BSRF-1W1A) using an x-ray wavelength of 1.54792 Å. The diffraction angles were calibrated using the NIST SRM660b (LaB6) standard.

Device characterization

The current density–voltage (*J-V*) curves and steady-state power output were recorded using a Keithley 2400 source-measurement unit under AM 1.5 G illumination (100 mW cm^{-2}) provided by an SS-F5-3A (Enlitech) solar simulator. The light intensity was calibrated using a certified silicon reference diode, and the spectral irradiance of the simulator was verified using a calibrated spectrometer. EQE spectra were collected using a QER Solar Cell Spectral Response Measurement System (Enli Technology Co. Ltd.). *J-V* curves of representative devices were obtained under both forward (−0.1 V → + 1.2 V) and reverse (+1.2 V → −0.1 V) scan directions.

TPV and TPC measurements

Transient Photovoltage (TPV) and Transient Photocurrent (TPC) measurements were carried out under a white-light bias generated by an array of LEDs (Molex 180081-4320) with an intensity of about 0.5 sun. A diode-pumped laser (Lapa-80) with a pulse duration of 10

Downloaded from https://www.science.org on June 07, 2026

ns and a repetition frequency of 20 Hz was used as the perturbation source. The perturbation light intensity was attenuated to maintain the transient V_{OC} below 10 mV. Voltage and current transients were recorded using a digital oscilloscope (Tektronix MDO4104C). Voltages under open-circuit conditions and currents under short-circuit conditions were obtained across 1 MΩ and 50 Ω resistors, respectively.

Trap density and mobility measurements

The trap-state density (N_t) of DJ perovskite films were performed by the space charge–limited current (SCLC) method. Measurements were performed in a hole-only device configuration of ITO/NiO_x/SA (or CA)/perovskite/spiro-OMeTAD/MoO_3/Ag. Dark current density–voltage curves were recorded in the voltage range of 0 to 4 V and fitted using an SCLC model.

Supplementary Materials

This PDF file includes:

Figs. S1 to S27
Tables S1 to S6
References

REFERENCES

1. X. Li, J. M. Hoffman, M. G. Kanatzidis, The 2D halide perovskite rulebook: How the spacer influences everything from the structure to optoelectronic device efficiency. *Chem. Rev.* **121**, 2230–2291 (2021).
2. G. Grancini, M. K. Nazeeruddin, Dimensional tailoring of hybrid perovskites for photovoltaics. *Nat. Rev. Mater.* **4**, 4–22 (2019).
3. B. Saparov, D. B. Mitzi, Organic-inorganic perovskites: Structural versatility for functional materials design. *Chem. Rev.* **116**, 4558–4596 (2016).
4. X. Zhao, T. Liu, Y.-L. Loo, Advancing 2D perovskites for efficient and stable solar cells: Challenges and opportunities. *Adv. Mater.* **34**, e2105849 (2021).
5. L. N. Quan, M. Yuan, R. Comin, O. Voznyy, E. M. Beauregard, S. Hoogland, A. Buin, A. R. Kirmani, K. Zhao, A. Amassian, D. H. Kim, E. H. Sargent, Ligand-stabilized reduced-dimensionality perovskites. *J. Am. Chem. Soc.* **138**, 2649–2655 (2016).
6. G. Wu, T. Liu, M. Hu, Z. Zhang, S. Li, L. Xiao, J. Guo, Y. Wang, A. Zhu, W. Li, H. Zhou, Y. Zhang, R. Chen, G. Xing, Crystallinity and phase control in formamidinium-based Dion-Jacobson 2D perovskite via seed-induced growth for efficient photovoltaics. *Adv. Mater.* **35**, e2303061 (2023).
7. Y.-C. Liu, J.-T. Lin, Y.-L. Lee, C.-M. Hung, T.-C. Chou, W.-C. Chao, Z.-X. Huang, T.-H. Chiang, C.-W. Chiu, W.-T. Chuang, P.-T. Chou, Recognizing the importance of fast nonisothermal crystallization for high-performance two-dimensional Dion-Jacobson perovskite solar cells with high fill factors: A comprehensive mechanistic Study. *J. Am. Chem. Soc.* **144**, 14897–14906 (2022).
8. X. Zhang, T. Yang, X. Ren, L. Zhang, K. Zhao, S. Liu, Film formation control for high performance Dion-Jacobson 2D perovskite solar cells. *Adv. Energy Mater.* **11**, 2002733 (2021).
9. Y. Dong, X. Dong, D. Lu, M. Chen, N. Zheng, R. Wang, Q. Li, Z. Xie, Y. Liu, Orbital interactions between the organic semiconductor spacer and the inorganic layer in Dion-Jacobson perovskites enable efficient solar cells. *Adv. Mater.* **35**, e2205258 (2023).
10. W. Zhang, Z. Liu, L. Zhang, H. Wang, C. Jiang, X. Wu, C. Li, S. Yue, R. Yang, H. Zhang, J. Zhang, X. Liu, Y. Zhang, H. Zhou, Ultrastable and efficient slight-interlayer-displacement 2D Dion-Jacobson perovskite solar cells. *Nat. Commun.* **15**, 5709 (2024).
11. Y. Liu, H. Zhou, Y. Ni, J. Guo, R. Lu, C. Li, X. Guo, Revealing stability origin of Dion-Jacobson 2D perovskites with different-rigidity organic cations. *Joule* **7**, 1016–1032 (2023).
12. T. Niu, H. Ren, B. Wu, Y. Xia, X. Xie, Y. Yang, X. Gao, Y. Chen, W. Huang, Reduced-dimensional perovskite enabled by organic diamine for efficient photovoltaics. *J. Phys. Chem. Lett.* **10**, 2349–2356 (2019).
13. T. He, S. Li, Y. Jiang, C. Qin, M. Cui, L. Qiao, H. Xu, J. Yang, R. Long, H. Wang, M. Yuan, Reduced-dimensional perovskite photovoltaics with homogeneous energy landscape. *Nat. Commun.* **11**, 1672 (2020).
14. H. Wu, X. Lian, J. Li, Y. Zhang, G. Zhou, X. Wen, Z. Xie, H. Zhu, G. Wu, H. Chen, Merged interface construction toward ultra-low V_{oc} loss in inverted two-dimensional Dion-Jacobson perovskite solar cells with efficiency over 18%. *J. Mater. Chem. A* **9**, 12566–12573 (2021).
15. C. Katan, N. Mercier, J. Even, Quantum and dielectric confinement effects in lower-dimensional hybrid perovskite semiconductors. *Chem. Rev.* **119**, 3140–3192 (2019).
16. Z. Xu, D. Lu, X. Dong, M. Chen, Q. Fu, Y. Liu, Highly efficient and stable Dion-Jacobson perovskite solar cells enabled by extended π-conjugation of organic spacer. *Adv. Mater.* **33**, e2105083 (2021).
17. J. Gong, M. Hao, Y. Zhang, M. Liu, Y. Zhou, Layered 2D halide perovskites beyond the Ruddlesden-Popper phase: Tailored interlayer chemistries for high-performance solar cells. *Angew. Chem. Int. Ed. Engl.* **61**, e202112022 (2022).
18. Y. Gao, X. Dong, Y. Liu, Recent progress of layered perovskite solar cells incorporating aromatic spacers. *Nano Micro Lett.* **15**, 169 (2023).
19. X. Dong, M. Chen, R. Wang, Q. Ling, Z. Hu, H. Liu, Y. Xin, Y. Yang, J. Wang, Y. Liu, Quantum confinement breaking: Orbital coupling in 2D Ruddlesden-Popper perovskites enables efficient solar cells. *Adv. Energy Mater.* **13**, 2301006 (2023).
20. X. Dong, H. Zhang, J. Li, L. Yang, Y. Ma, H. Liu, Z. Hu, Y. Liu, Semiconductor spacer with donor-acceptor structure drives 2D Ruddlesden-Popper perovskite solar cells beyond 20% efficiency. *Angew. Chem. Int. Ed. Engl.* **64**, e202501210 (2025).
21. J. Sun, K. Wang, K. Ma, J. Y. Park, Z.-Y. Lin, B. M. Savoie, L. Dou, Emerging two-dimensional organic semiconductor-incorporated perovskites–A fascinating family of hybrid electronic materials. *J. Am. Chem. Soc.* **145**, 20694–20715 (2023).
22. R. Zhao, R. P. Sabatini, T. Zhu, S. Wang, A. M. Najjarian, A. Johnston, A. J. Lough, S. Hoogland, E. H. Sargent, D. S. Seferos, Rigid conjugated diamine templates for stable Dion-Jacobson-type two-dimensional perovskites. *J. Am. Chem. Soc.* **143**, 19901–19908 (2021).
23. F. Zhang, D. H. Kim, H. Lu, J.-S. Park, B. W. Larson, J. Hu, L. Gao, C. Xiao, O. G. Reid, X. Chen, Q. Zhao, P. F. Ndione, J. J. Berry, W. You, A. Walsh, M. C. Beard, K. Zhu, Enhanced charge transport in 2D perovskites via fluorination of organic cation. *J.Am. Chem. Soc.* **141**, 5972–5979 (2019).
24. H. Tsai, W. Nie, J.-C. Blancon, C. C. Stoumpos, R. Asadpour, B. Harutyunyan, A. J. Neukirch, R. Verduzco, J. J. Crochet, S. Tretiak, L. Pedesseau, J. Even, M. A. Alam, G. Gupta, J. Lou, P. M. Ajayan, M. J. Bedzyk, M. G. Kanatzidis, A. D. Mohite, High-efficiency two-dimensional Ruddlesden-Popper perovskite solar cells. *Nature* **536**, 312–316 (2016).
25. W. Ke, L. Mao, C. C. Stoumpos, J. Hoffman, I. Spanopoulos, A. D. Mohite, M. G. Kanatzidis, Compositional and solvent engineering in Dion-Jacobson 2D perovskites boosts solar cell efficiency and stability. *Adv. Energy Mater.* **9**, 1803384 (2019).
26. H. Lai, B. Kan, T. Liu, N. Zheng, Z. Xie, T. Zhou, X. Wan, X. Zhang, Y. Liu, Y. Chen, Two-dimensional Ruddlesden-Popper perovskite with nanorod-like morphology for solar cells with efficiency exceeding 15%. *J. Am. Chem. Soc.* **140**, 11639–11646 (2018).
27. X. Zhang, G. Wu, S. Yang, W. Fu, Z. Zhang, C. Chen, W. Liu, J. Yan, W. Yang, H. Chen, Vertically oriented 2D layered perovskite solar cells with enhanced efficiency and good stability. *Small* **13**, 1700611 (2017).
28. L. Cheng, Z. Liu, S. Li, Y. Zhai, X. Wang, Z. Qiao, Q. Xu, K. Meng, Z. Zhu, G. Chen, Highly thermostable and efficient formamidinium-based low-dimensional perovskite solar cells. *Angew. Chem. Int. Ed. Engl.* **60**, 856–864 (2021).
29. D. Lu, G. Lv, Z. Xu, Y. Dong, X. Ji, Y. Liu, Thiophene-based two-dimensional Dion-Jacobson perovskite solar cells with over 15% efficiency. *J. Am. Chem. Soc.* **142**, 11114–11122 (2020).
30. X. Zhao, T. Liu, A. B. Kaplan, C. Yao, Y. L. Loo, Accessing highly oriented two-dimensional perovskite films via solvent-vapor annealing for efficient and stable solar cells. *Nano Lett.* **20**, 8880–8889 (2020).
31. H. Wu, J. Wu, Z. Zhang, X. Guan, L. Wang, L.-L. Deng, G. Li, A. Abate, M. Li, Tailored lattice-matched carbazole self-assembled molecule for efficient and stable perovskite solar cells. *J. Am. Chem. Soc.* **147**, 8004–8011 (2025).
32. G. Liu, G. Yang, W. Feng, H. Li, M. Yang, Y. Zhong, X. Jiang, W.-Q. Wu, Regulating surface metal abundance via lattice-matched coordination for versatile and environmentally-viable Sn-Pb alloying perovskite solar cells. *Adv. Mater.* **36**, e2405860 (2024).
33. X. Wang, H. Huang, M. Wang, Z. Lan, P. Cui, S. Du, Y. Yang, L. Yan, Q. Zhang, S. Qu, M. Li, Oriented molecular bridge constructs homogeneous buried interface for perovskite solar cells with efficiency over 25.3%. *Adv. Mater.* **36**, e2310710 (2024).
34. H. Guo, W. Xiang, Y. Fang, J. Li, Y. Lin, Molecular bridge on buried interface for efficient and stable perovskite solar cells. *Angew. Chem. Int. Ed. Engl.* **62**, e202304568 (2023).
35. M. Du, S. Zhao, L. Duan, Y. Cao, H. Wang, Y. Sun, L. Wang, X. Zhu, J. Feng, L. Liu, X. Jiang, Q. Dong, Y. Shi, K. Wang, S. F. Liu, Surface redox engineering of vacuum-deposited NiO_x for top-performance perovskite solar cells and modules. *Joule* **6**, 1931–1943 (2022).
36. C. Liu, T. Yang, W. Cai, Y. Wang, X. Chen, S. Wang, W. Huang, Y. Du, N. Wu, Z. Wang, Y. Yang, J. Feng, T. Niu, Z. Ding, K. Zhao, Flexible Indoor perovskite solar cells by in situ bottom-up crystallization modulation and interfacial passivation. *Adv. Mater.* **36**, e2311562 (2024).
37. J. M. Hoffman, J. Strzalka, N. C. Flanders, I. Hadar, S. A. Cuthriell, Q. Zhang, R. D. Schaller, W. R. Dichtel, L. X. Chen, M. G. Kanatzidis, In situ grazing-incidence wide-angle scattering reveals mechanisms for phase distribution and disorientation in 2D halide perovskite films. *Adv. Mater.* **32**, e2002812 (2020).
38. T. Lv, Y. Liang, F. Li, X. Yang, J. Huang, R. Zheng, Two-dimensional halide perovskites: A review on their orientations. *Sci. China Phys. Mech. Astron.* **66**, 217306 (2023).
39. Q. Cao, T. Wang, X. Pu, X. He, M. Xiao, H. Chen, L. Zhuang, Q. Wei, H.-L. Loi, P. Guo, B. Kang, G. Feng, J. Zhuang, G. Feng, X. Li, F. Yan, Co-self-assembled monolayers modified NiO_x for stable inverted perovskite solar cells. *Adv. Mater.* **36**, e2311970 (2024).
40. L. Yang, H. Zhou, Y. Duan, M. Wu, K. He, Y. Li, D. Xu, H. Zou, S. Yang, Z. Fang, S. Liu, Z. Liu, 25.24%-efficiency $FACsPbI_3$ perovskite solar cells enabled by intermolecular esterification reaction of DL-carnitine hydrochloride. *Adv. Mater.* **35**, e2211545 (2023).

Downloaded from https://www.science.org on June 07, 2026

41. X. Dong, R. Wang, Y. Gao, Q. Ling, Z. Hu, M. Chen, H. Liu, Y. Liu, Orbital interactions in 2D Dion-Jacobson perovskites using oligothiophene-based semiconductor spacers enable efficient solar cells. *Nano Lett.* **24**, 261–269 (2023).
42. J. Zhang, J. Yang, R. Dai, W. Sheng, Y. Su, Y. Zhong, X. Li, L. Tan, Y. Chen, Elimination of interfacial lattice mismatch and detrimental reaction by self-assembled layer dual-passivation for efficient and stable inverted perovskite solar cells. *Adv. Energy Mater.* **12**, 2103674 (2022).
43. R. L. Z. Hoye, J. Hidalgo, R. A. Jagt, J.-P. Correa-Baena, T. Fix, J. L. MacManus-Driscoll, The role of dimensionality on the optoelectronic properties of oxide and halide perovskites, and their halide derivatives. *Adv. Energy Mater.* **12**, 2100499 (2022).
44. C. Luo, G. Zheng, F. Gao, X. Wang, C. Zhan, X. Gao, Q. Zhao, Engineering the buried interface in perovskite solar cells via lattice-matched electron transport layer. *Nat. Photonics* **17**, 856–864 (2023).
45. M. Shao, T. Bie, L. Yang, Y. Gao, X. Jin, F. He, N. Zheng, Y. Yu, X. Zhang, Over 21% efficiency stable 2D perovskite solar cells. *Adv. Mater.* **34**, e2107211 (2022).
46. F. Zeng, W. Kong, Y. Liang, F. Li, Y. Lvtao, Z. Su, T. Wang, B. Peng, L. Ye, Z. Chen, X. Gao, J. Huang, R. Zheng, X. Yang, Highly stable and efficient formamidinium-based 2D Ruddlesden-Popper perovskite solar cells via lattice manipulation. *Adv. Mater.* **35**, e2306051 (2023).
47. H. Ren, S. Yu, L. Chao, Y. Xia, Y. Sun, S. Zuo, F. Li, T. Niu, Y. Yang, H. Ju, B. Li, H. Du, X. Gao, J. Zhang, J. Wang, L. Zhang, Y. Chen, W. Huang, Efficient and stable Ruddlesden-Popper perovskite solar cell with tailored interlayer molecular interaction. *Nat. Photonics* **14**, 154–163 (2020).
48. I. C. Smith, E. T. Hoke, D. Solis-Ibarra, M. D. McGehee, H. I. Karunadasa, A layered hybrid perovskite solar-cell absorber with enhanced moisture stability. *Angew. Chem. Int. Ed. Engl.* **53**, 11232–11235 (2014).
49. Y. Dong, D. Lu, Z. Xu, H. Lai, Y. Liu, 2-Thiopheneformamidinium-based 2D Ruddlesden-Popper perovskite solar cells with efficiency of 16.72% and negligible hysteresis. *Adv. Energy Mater.* **10**, 202000694 (2020).
50. Z. Xu, D. Lu, F. Liu, H. Lai, X. Wan, X. Zhang, Y. Liu, Y. Chen, Phase distribution and carrier dynamics in multiple-ring aromatic spacer-based two-dimensional Ruddlesden-Popper perovskite solar cells. *ACS Nano* **14**, 4871–4881 (2020).
51. G. Wu, X. Li, J. Zhou, J. Zhang, X. Zhang, X. Leng, P. Wang, M. Chen, D. Zhang, K. Zhao, S. F. Liu, H. Zhou, Y. Zhang, Fine multi-phase alignments in 2D perovskite solar cells with efficiency over 17% via slow post-annealing. *Adv. Mater.* **31**, e1903889 (2019).
52. J. Shi, Y. Gao, X. Gao, Y. Zhang, J. Zhang, X. Jing, M. Shao, Fluorinated low-dimensional Ruddlesden-Popper perovskite solar cells with over 17% power conversion efficiency and improved stability. *Adv. Mater.* **31**, e1901673 (2019).
53. Q. Li, Y. Dong, G. Lv, T. Liu, D. Lu, N. Zheng, X. Dong, Z. Xu, Z. Xie, Y. Liu, Fluorinated aromatic formamidinium spacers boost efficiency of layered Ruddlesden-Popper perovskite solar cells. *ACS Energy Lett.* **6**, 2072–2080 (2021).
54. Z. Wang, Q. Wei, X. Liu, L. Liu, X. Tang, J. Guo, S. Ren, G. Xing, D. Zhao, Y. Zheng, Spacer cation tuning enables vertically oriented and graded quasi-2D perovskites for efficient solar cells. *Adv. Funct. Mater.* **31**, 2008404 (2021).
55. R. Yang, R. Li, Y. Cao, Y. Wei, Y. Miao, W. L. Tan, X. Jiao, H. Chen, L. Zhang, Q. Chen, H. Zhang, W. Zou, Y. Wang, M. Yang, C. Yi, N. Wang, F. Gao, C. R. McNeill, T. Qin, J. Wang, W. Huang, Oriented quasi-2D perovskites for high performance optoelectronic devices. *Adv. Mater.* **30**, e1804771 (2018).
56. Y. Yang, C. Liu, O. A. Syzgantseva, M. A. Syzgantseva, S. Ma, Y. Ding, M. Cai, X. Liu, S. Dai, M. K. Nazeeruddin, Defect suppression in oriented 2D perovskite solar cells with efficiency over 18% via rerouting crystallization pathway. *Adv. Energy Mater.* **11**, 2002966 (2021).
57. H. Lai, D. Lu, Z. Xu, N. Zheng, Z. Xie, Y. Liu, Organic-Salt-assisted crystal growth and orientation of quasi-2D Ruddlesden-Popper perovskites for solar cells with efficiency over 19%. *Adv. Mater.* **32**, e2001470 (2020).
58. Q. Fu, M. Chen, Q. Li, H. Liu, R. Wang, Y. Liu, Selenophene-based 2D Ruddlesden-Popper perovskite solar cells with an efficiency exceeding 19%. *J. Am. Chem. Soc.* **145**, 21687–21695 (2023).
59. R. Wang, X. Dong, Q. Ling, Z. Hu, Y. Gao, Y. Chen, Y. Liu, Nucleation and crystallization in 2D Ruddlesden-Popper perovskites using formamidinium-based organic semiconductor spacers for efficient solar cells. *Angew. Chem. Int. Ed. Engl.* **62**, e202314690 (2023).
60. J. H. Kim, C. M. Oh, I. W. Hwang, J. Kim, C. Lee, S. Kwon, T. Ki, S. Lee, H. Kang, H. Kim, K. Lee, Efficient and stable quasi-2D Ruddlesden-Popper perovskite solar cells by tailoring crystal orientation and passivating surface defects. *Adv. Mater.* **35**, e2302143 (2023).
61. Z. Pan, D. Peng, X. Zhao, W. Xu, Y. Bao, Z. Feng, Q. Zou, B. Xu, Y. Wang, H. Gao, C. Yin, R. Li, J. Wang, W. Huang, Side-chain functionalized polymer hole-transporting materials with defect passivation effect for highly efficient inverted quasi-2D perovskite solar cells. *Adv. Funct. Mater.* **33**, 2304881 (2023).
62. Y. Li, J. V. Milić, A. Ummadisingu, J.-Y. Seo, J.-H. Im, H.-S. Kim, Y. Liu, M. I. Dar, S. M. Zakeeruddin, P. Wang, A. Hagfeldt, M. Grätzel, Bifunctional organic spacers for formamidinium-based hybrid Dion-Jacobson two-dimensional perovskite solar cells. *Nano Lett.* **19**, 150–157 (2019).
63. X. Li, W. Ke, B. Traoré, P. Guo, I. Hadar, M. Kepenekian, J. Even, C. Katan, C. C. Stoumpos, R. D. Schaller, M. G. Kanatzidis, Two-dimensional Dion-Jacobson hybrid lead iodide perovskites with aromatic diammonium cations. *J. Am. Chem. Soc.* **141**, 12880–12890 (2019).
64. G. Lv, L. Li, D. Lu, Z. Xu, Y. Dong, Q. Li, Z. Chang, W. Yin, Y. Liu, Multiple-noncovalent-interaction-stabilized layered Dion-Jacobson perovskite for efficient solar cells. *Nano Lett.* **21**, 5788–5797 (2021).
65. O. Almora, C. Aranda, E. Mas-Marza, G. Garcia-Belmonte, On Mott-Schottky analysis interpretation of capacitance measurements in organometal perovskite solar cells. *Appl. Phys. Lett.* **109**, 173903 (2016).
66. V. D. Mihailetchi, J. Wildeman, P. W. M. Blom, Space-charge limited photocurrent. *Phys. Rev. Lett.* **94**, 126602 (2005).
67. J. Zhu, Y. Luo, R. He, C. Chen, Y. Wang, J. Luo, Z. Yi, J. Thiesbrummel, C. Wang, F. Lang, H. Lai, Y. Xu, J. Wang, Z. Zhang, W. Liang, G. Cui, S. Ren, X. Hao, H. Huang, Y. Wang, F. Yao, Q. Lin, L. Wu, J. Zhang, M. Stolterfoht, F. Fu, D. Zhao, A donor-acceptor-type hole-selective contact reducing non-radiative recombination losses in both subcells towards efficient all-perovskite tandems. *Nat. Energy* **8**, 714–724 (2023).
68. S. Wang, Y. Li, J. Yang, T. Wang, B. Yang, Q. Cao, X. Pu, L. Etgar, J. Han, J. Zhao, X. Li, A. Hagfeldt, Critical role of removing impurities in nickel oxide on high-efficiency and long-term stability of inverted perovskite solar cells. *Angew. Chem. Int. Ed. Engl.* **61**, e202116534 (2022).
69. C. C. Boyd, R. C. Shallcross, T. Moot, R. Kerner, L. Bertoluzzi, A. Onno, S. Kavadiya, C. Chosy, E. J. Wolf, J. Werner, J. A. Raiford, C. de Paula, A. F. Palmstrom, Z. S. J. Yu, J. J. Berry, S. F. Bent, Z. C. Holman, J. M. Luther, E. L. Ratcliff, N. R. Armstrong, M. D. McGehee, Overcoming redox reactions at perovskite-nickel oxide interfaces to boost voltages in perovskite solar cells. *Joule* **4**, 1759–1775 (2020).
70. P. Kovaricek, P. Nadazdy, E. Pluharova, A. Brunova, R. Subair, K. Vegso, V. L. P. Guerra, O. Volochanskyi, M. Kalbac, A. Krasnansky, P. Pandit, S. V. Roth, A. Hinderhofer, E. Majkova, M. Jergel, J. J. Tian, F. Schreiber, P. Siffalovic, Crystallization of 2D hybrid organic-inorganic perovskites templated by conductive substrates. *Adv. Funct. Mater.* **31**, 2009007 (2021).
71. X. Zheng, Y. Hou, C. Bao, J. Yin, F. Yuan, Z. Huang, K. Song, J. Liu, J. Troughton, N. Gasparini, C. Zhou, Y. Lin, D.-J. Xue, B. Chen, A. K. Johnston, N. Wei, M. N. Hedhili, M. Wei, A. Y. Alsalloum, P. Maity, B. Turedi, C. Yang, D. Baran, T. D. Anthopoulos, Y. Han, Z.-H. Lu, O. F. Mohammed, F. Gao, E. H. Sargent, O. M. Bakr, Managing grains and interfaces via ligand anchoring enables 22.3%-efficiency inverted perovskite solar cells. *Nat. Energy* **5**, 131–140 (2020).

Acknowledgments: We thank H. P. Zhou at Peking University for insightful discussions and valuable feedback on the manuscript. We also acknowledge the beam time provided by the 1W1A station (Beijing Synchrotron Radiation Facility) for support with the GIWAXS characterization. In addition, we acknowledge the use of Xeuss 3.0 (Xenocs Company, France) at the Institute of Polymer Chemistry, Nankai University, for GIWAX analysis. **Funding:** The authors gratefully acknowledge the financial support from the National Natural Science Foundation of China (grant nos. 22479121 and 52273182) and the Haihe Laboratory of Sustainable Chemical Transformations (grant no. 25HHWCSS00031). **Author contributions:** Conceptualization: Y.L. and Yongsheng Chen. Methodology: R.W., Y.L., and Yongsheng Chen. Investigation: R.W., X.D., Y.M., L.Y., J.L., Y.G., Yu Chen, W.F., Z.H., and Yongsheng Chen. Visualization: RW and Y.L.. Resources: Y.L., Yongsheng Chen, Yu Chen, Y.Z., and Z.H.. Validation: Yongsheng Chen . Supervision: Y.L. and Yongsheng Chen. Project administration: Y.L. and Yongsheng Chen. Writing—original draft: R.W. and Yongsheng Chen. Writing—review and editing: Y.L. and Yongsheng Chen. Funding acquisition: Y.L. and Yongsheng Chen. **Competing interests:** Y.L. and R.W. are inventors on a patent application (application no. 202310908246.8) filed on 24 July, 2023 by Nankai University that covers the CA- and SA-based interface layers and the related devices. The other authors declare that they have no competing interests. **Data, code, and materials availability:** All data and code needed to evaluate and reproduce the results in the paper are present in the paper and/or the Supplementary Materials. This study did not generate new materials.

Submitted 17 July 2025
Accepted 13 April 2026
Published 22 May 2026
10.1126/sciadv.aea7043

Downloaded from https://www.science.org on June 07, 2026

ScienceAdvances

Molecular interfaces drive vertical crystallization in Dion-Jacobson perovskite solar cells

Rui Wang, Xiyue Dong, Yuting Ma, Liu Yang, Jiangnan Li, Yuping Gao, Yu Chen, Yu Zou, Wenjuan Feng, Ziyang Hu, Yongsheng Chen, and Yongsheng Liu

Sci. Adv. **12** (21), eaea7043. DOI: 10.1126/sciadv.aea7043

View the article online
https://www.science.org/doi/10.1126/sciadv.aea7043
Permissions
https://www.science.org/help/reprints-and-permissions

Downloaded from https://www.science.org on June 07, 2026

Use of this article is subject to the Terms of service

Science Advances (ISSN 2375-2548) is published by the American Association for the Advancement of Science. 1200 New York Avenue NW, Washington, DC 20005. The title *Science Advances* is a registered trademark of AAAS.

Copyright © 2026 The Authors, some rights reserved; exclusive licensee American Association for the Advancement of Science. No claim to original U.S. Government Works. Distributed under a Creative Commons Attribution NonCommercial License 4.0 (CC BY-NC).